AIAA 2001-3589

Cold-Flow Analysis of the Gas Dynamics in a Slab Rocket Motor Including Curvature Effects

J. Majdalani
Marquette University
Milwaukee, WI 53233

W. K. Van Moorhem
University of Utah
Salt Lake City, UT 84112

37th AIAA/ASME/SAE/ASEE Joint Propulsion Conference and Exhibit
8–11 July 2001, Salt Lake City, UT

Cold-Flow Analysis of the Gas Dynamics in a Slab Rocket Motor Including Curvature Effects

J. Majdalani*
Marquette University, Milwaukee, WI 53233
and
W. K. Van Moorhem†
University of Utah, Salt Lake City, UT 84112

This paper considers the internal fluid dynamics of the slab rocket motor based on a laminar cold-flow model. An idealization process applicable to nonreacting flows leads to a mathematical solution for both steady and unsteady flow variables. Results are compared to the circular-port solution. This brings into focus the effect of a motor's radius of curvature. By comparison to a circular grain, a planar cross section exhibits slower and more gradual flow turning near the wall. It also induces reductions in core velocities and vorticities by ½ and ¼, respectively. On the one hand, it appears that the reduced vortical intensity could make the slab configuration more resilient to vibrations and acoustic combustion instabilities. On the other hand, decreasing the radius of curvature seems to inhibit the inward penetration of vorticity. By comparison with the circular port, the simulated slab exhibits a more spatially uniform pressure and an uneven mass efflux at the aft end. Since the mass efflux is concentrated in a thin sheet near the core, the slab configuration is likely to exhibit improved stealth capabilities. The temporal solution is derived using the composite-scale and multiple-order WKB techniques. Asymptotic results are validated via comparisons with finite-volume solutions of the complete Navier-Stokes equations. Simulated conditions apply to forward motor segments and planar cold-flow experiments.

I. Introduction

THIS paper focuses on analyzing the internal fluid dynamics for the slab rocket motor configuration featuring a rectangular cross section. The derivation to be pursued corresponds to the basic nonturbulent structure that persists outside of the propellant's flame zone. To be precise, the analysis will concentrate on the strong coupling between acoustical and vortical waves caused by the oscillatory motion above the propellant surface. The solution sought applies to weakly reactive and non-reactive working fluids. It features the laminar, cold-flow regime that exists when entropy mode disturbances are suppressed. The latter, when present, can drastically alter the flow character whereby a separate treatment may be warranted. Only pressure-driven and boundary-driven disturbances will be considered here. Inasmuch as thermal disturbances are omitted, the desired formulation will reminisce of an 'outer' perturbation solution. Imposition of thermal fluctuations is hoped to be accomplished in a forthcoming study. The purpose of an outer solution is dual. First, it is to provide a valid internal flow model for non-reactive, cold-flow applications. Second, it is to serve as the leading-order term in a perturbation scheme that incorporates thermal disturbances caused by unsteady propellant combustion.

Most analytical work in the past has addressed axisymmetric flow structures in circular-port geometries. Such configurations mimic commonly produced rocket motors (see for example Culick,[1] Flandro,[2-6] Majdalani and Van Moorhem,[7,8] and Kirkkopru et al.[9]). Much can be gained from these traditional idealizations that produce closed-form solutions. Flow features precipitated by analytical models have been often substantiated by testing or exploited in the design and planning of experiments.

In extending traditional idealizations, the current analysis focuses on the flow structure in a less familiar geometry. This is done for three principal reasons. First, to provide an explicit cold-flow solution to which comparisons can be drawn. Second, to explore the effects that a chamber's radius of curvature can have on altering the vortical flow structure. Third, to provide a more accurate flowfield approximation than the one-

*Assistant Professor, Department of Mechanical and Industrial Engineering. Member AIAA.
†Professor, Mechanical Engineering Department. Senior Member AIAA.

dimensional or incomplete two-dimensional plane wave solutions used to predict stability during motor firings.

The first motivation stems from the need to provide a formal theoretical formulation to which experimental and numerical data obtained in rectangular chambers can be compared. The reader may consult with the works of Barron et al.,[10,11] Brownlee and Marble,[12] Ma et al.,[13-16] Rao et al.,[17] Apte and Yang,[18] Traineau et al.,[19] Avalon et al.,[20] and Casalis et al.[21] These studies have utilized rectangular test chambers with transpiring walls. The second motivation regards assessing advantages and disadvantages of circular versus rectangular configurations. This is inspired by scientific curiosity. The third motivation, undoubtedly, is aimed at improving the tools we possess for predicting acoustic stability and its impact on rocket performance.

The paper is organized in the following manner: First, the system parameters such as geometry and principal variables are defined. The range for meaningful physical settings is stated as well. Second, the governing Navier-Stokes equations are presented along with required assumptions. In Sec. III, linearized equations are obtained from separating the flow into a steady component and a time-dependent fluctuation. While the solution to the steady component is presented in Sec. IV, the unsteady flowfield is separated into two independent and linearly superimposable solutions in Sec. V. This subdivides the field into acoustic and vortical parts. The solution to the acoustic, or so-called lamellar component of the flow, is obtained to the order of the surface Mach number. The vortical or so-called solenoidal component of the flow is addressed in the remaining analysis. Thus, in Sec. VI, the rotational and viscous solution is formulated. The procedure employs a multiple-scale perturbation solution presented recently by the authors.[8] Furthermore, a formal WKB solution is constructed to provide a separate asymptotic formulation that is valid to any desired order. In Sec. VII, a discussion of the resulting flow structure is presented. Whenever possible, a confirmatory analysis is carried out offering comparisons with reliable numerical solutions. Our numerical simulations rely on two separate sources: (1) a finite difference solution of the linearized Navier-Stokes equations (produced by the authors), and (2) an independent finite-volume solution of the nonlinear Navier-Stokes equations furnished by Yang and Cai.[22] The latter is based on a code that was first developed by Roh and co-workers.[23] It should be noted that the main steps leading to the fundamental solution follow closely those presented by Majdalani and Van Moorhem[8] for the cylindrical motor. The novelty in the present article lies in (1) the formal derivation of the WKB solution to any desired order, (2) the disclosure of the problem's nonlinear scaling structure, and (3) the comparative study addressing the curvature effect or lack thereof.

II. Idealization

In defining the solution domain, we consider a rectangular chamber of length L_0, width W_0, and height $2h_0$ ($L_0 >> h_0$). A transverse gas flux of kinematic viscosity ν_0 crosses the bottom wall ($y=0$) at a uniform blowing speed V_0. Using asterisks to denote dimensional quantities, the coordinates shown in Fig. 1 are $y = y^*/h_0$ and $z = z^*/h_0$. These represent the normalized vertical and axial distances measured, respectively, from the bottom and head-end walls. The chamber is rigid at the head end and is attached to either a) a choked nozzle (not shown) or b) an isobaric opening at the downstream end. The lateral walls perpendicular to the x axis are rigid as well. Since we are interested in the two-dimensional flow character away from the impenetrable walls, we assume sufficiently large chamber width to neglect variations in the x direction. This assumption is justified by virtue of the very thin Stokes layer forming along the rigid walls. In the absence of oscillatory motions, the gas entering the chamber from the transpiring wall turns and heads downstream (Fig. 1). When small amplitude acoustic waves (of frequency ω_0 and pressure amplitude A_0) are generated inside the chamber, a complex time-dependent field ensues. This field is a direct consequence of the steady field interaction with both pressure and vorticity wave motions. Depending on whether the downstream end is acoustically closed or open, the longitudinal frequency will be

$$\omega_0 = \begin{cases} m\pi a_0/L_0 & (a) \\ (m-\tfrac{1}{2})\pi a_0/L_0 & (b) \end{cases}, \quad k_m = \begin{cases} m\pi h_0/L_0 & (a) \\ (m-\tfrac{1}{2})\pi h_0/L_0 & (b) \end{cases} \tag{1}$$

where m and k_m are the dimensionless oscillation mode and wave numbers. Due to symmetry about the midsection plane (labeled, hereafter, as the 'core'), our field investigation will be confined to $0 \le y \le 1$.

III. Mathematical Model

A. Mass and Momentum Conservation

In seeking an analytical solution to the internal field, the Stokes hypothesis is assumed, viscosity is held constant throughout the field, and body forces are

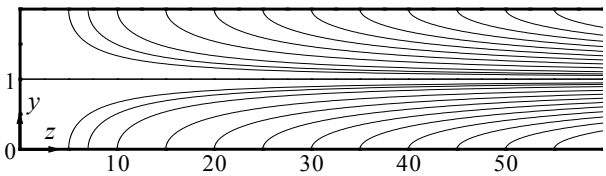

Fig. 1 Chamber geometry and mean flow streamlines.

ignored. When this is done, the Navier-Stokes equations reduce to the familiar set

$$\partial\rho/\partial t + \nabla.(\rho\boldsymbol{u}) = 0 \tag{2}$$

$$\rho D\boldsymbol{u}/Dt + \nabla p = \delta^2\left[(4/3)\nabla(\nabla.\boldsymbol{u}) - \nabla\times(\nabla\times\boldsymbol{u})\right] \tag{3}$$

where

$$p = \frac{p^*}{\gamma p_0},\ \rho = \frac{\rho^*}{\rho_0},\ t = \frac{t^* a_0}{h_0},\ \boldsymbol{u} = \frac{\boldsymbol{u}^*}{a_0},\ \gamma = \frac{C_p}{C_v},\ \delta^2 = \frac{\nu_0}{a_0 h_0} \tag{4}$$

Here ρ_0 and p_0 are the mean stagnation density and pressure evaluated at the rigid head end. Remaining terms have their usual significance.

B. Limiting Assumptions

Fundamental conditions that must be satisfied are stipulated here. The first requirement is that of a small wall Mach number satisfying $M = V_0/a_0 \ll 1$. This requirement is justified in many physical settings. For example, in typical cold-flow experiments, the isentropic speed of sound is about 340 m/s, while blowing velocities are of the order of few centimeters per second. This generates a Mach number of $O(10^{-3})$. In actual rockets, the speed of sound is higher by an order of magnitude while burning rates do not usually produce blowing velocities that exceed 7 m/s. The second condition needed to linearize the conservation equations requires a small ε_0, where $\varepsilon_0 = A_0/(\gamma p_0)$. According to classic acoustic stability theory, one must posit $M^2 < \varepsilon_0 < M$. For large wall injection, these parameters must be consistent with

$$\lim_{\varepsilon_0, M\to 0}\frac{\varepsilon_0}{M} = 0,\quad \lim_{\delta^2, M\to 0}\frac{\delta^2}{M} = 0 \tag{5}$$

Note that $\delta^2 M^{-1} \equiv \varepsilon$ is the reciprocal of the commonly used crossflow Reynolds number $R \equiv V_0 h_0/\nu_0$.

C. Expansion of Primary Variables

Following Flandro's lead,[3] the total normalized pressure, density and pressure can be written as the composite sum of steady and time-dependent parts:

$$p = 1/\gamma + \varepsilon_0 p^{(1)}\exp(-ik_m t),$$
$$\rho = 1 + \varepsilon_0\rho^{(1)}\exp(-ik_m t),$$
$$\boldsymbol{u} = M\boldsymbol{U}(y,z) + \varepsilon_0\boldsymbol{u}^{(1)}(y,z,t)\exp(-ik_m t) \tag{6}$$

where $\boldsymbol{U}$ is a function of $O(1)$ that will be described in Sec. IV.

D. Linearized Navier-Stokes Equations

Next we insert the perturbed variables in their dimensionless form back into Eqs. (2)–(3). As we expand and collect terms of order $O(1)$, we obtain the set that prescribes the steady flow motion

$$\nabla.\boldsymbol{U} = 0 \tag{7}$$

$$M\left[\nabla(\boldsymbol{U}.\boldsymbol{U})/2 - \boldsymbol{U}\times(\nabla\times\boldsymbol{U})\right] = \delta^2\nabla^2\boldsymbol{U} \tag{8}$$

Collecting terms that are comparable in magnitude to the first order in the wave amplitude, we obtain the interaction equations that incorporate the strong coupling between mean and unsteady flow components

$$-ik_m\rho^{(1)} + \nabla.\boldsymbol{u}^{(1)} = -M\nabla.\left(\rho^{(1)}\boldsymbol{U}\right) \tag{9}$$

$$\nabla p^{(1)} - ik_m\boldsymbol{u}^{(1)} = M\left[\boldsymbol{u}^{(1)}\times\boldsymbol{\Omega} + \boldsymbol{U}\times\left(\nabla\times\boldsymbol{u}^{(1)}\right) - \nabla\left(\boldsymbol{u}^{(1)}.\boldsymbol{U}\right)\right] + \delta^2\left[\tfrac{4}{3}\nabla\left(\nabla.\boldsymbol{u}^{(1)}\right) - \nabla\times\left(\nabla\times\boldsymbol{u}^{(1)}\right)\right] \tag{10}$$

where $\boldsymbol{\Omega} = \nabla\times\boldsymbol{U} = \Omega\boldsymbol{e}_x$ is the mean flow vorticity vector.

IV. Steady Field

A. Classic Solution for Large Injection

Equations (7)–(8) can be reduced to Berman's equation[24] and then solved asymptotically following Yuan.[25] Defining the streamfunction to be of the Berman type, (i.e., that varies linearly with the distance from the head end due to geometric similarity) we let $\Psi(y,z) = zF(y)$. The companion velocities become $(U_y, U_z) = (F, -zF')$. For uniform injection along the wall, $U_y(0) = 1$. In addition, symmetry along the core and the no slip at the wall require that $U_y(1) = U_z'(1,z) = 0$, and $U_z(0,z) = 0$. Forthwith, Navier-Stokes equations reduce to

$$\varepsilon F'''' + F'F'' - FF''' = 0$$

with $F'(0) = F(1) = F''(1) = 0$, and $F(0) = 1$. (11)

Using regular perturbations, one can set $F = F_0 + \varepsilon F_1 + O(\varepsilon^2)$. Letting $\theta = \frac{\pi}{2}y$, $\phi = \frac{\pi}{2} - \theta$, $A = \frac{2}{\pi}\left[\mathrm{I}(\frac{\pi}{2}) - 1\right] \simeq 0.5296237$, and $\mathrm{I}(x) \equiv \int_0^x z\csc z\,\mathrm{d}z$, direct substitution into Eq. (11) gives

$$F = \sin\phi + (\pi/4)\varepsilon\left\{(\phi\cos\phi - \sin\phi)\ln\left|\tan(\phi/2)\right| + \cos\phi\left[A\phi - \mathrm{I}(\phi)\right]\right\} + O(\varepsilon^2); \tag{12}$$

$$\mathrm{I}(x) = x + 2\sum_{k=1}^{\infty}\pi^{-2k}\frac{\left(1-2^{1-2k}\right)}{(2k+1)}\left(\sum_{j=1}^{\infty}j^{-2k}\right)x^{2k+1}. \tag{13}$$

When compared with the inviscid solutions presented by Taylor[26] or Culick,[1] Eq. (12) provides an expansion that incorporates viscous corrections. For infinitely large R, $\varepsilon \to 0$, $F \to F_0$, and one retains the leading-order term only. For finite injection, however, the first-order corrections in Eq. (12) may be included to obtain an improved description of the mean flow. Evidently, the improved accuracy becomes appreciable when R is no longer large.

In order to minimize the forthcoming algebraic effort, the mean flow will be represented by F_0 in all intermediate steps. When the need arises, the final expressions that are function of F_0 and its derivatives

are replaced by F and its derivatives. Hence, at $O(\varepsilon)$, one may write

$$\Psi(y,z) = z\cos\theta\ ,\ \Omega = -zF'' = (\pi^2/4)z\cos\theta\ ,$$
$$\left(U_y, U_z\right) = \left(\cos\theta,\ \tfrac{\pi}{2} z\sin\theta\right) \qquad (14)$$

B. Mean Flow Character

The leading order-term in Eq. (12) is similar to the Taylor or Culick axisymmetric profiles.[1] As with the circular port, the planar mean flow is characterized by a linear increase in both axial velocity and vorticity with increasing distance from the head end. In a rectangular chamber, however, the curvature effects are removed. At the outset, the core velocity $(\pi z V_0/2)$ at any axial distance z is precisely one half of its counterpart $(\pi z V_0)$ in a comparable circular chamber (with effective radius $r_0 = h_0$). This reinforces the effectiveness of a circular chamber in achieving higher core velocities for the same injection velocity and mean chamber pressure. In practice, establishing the same injection velocity, chamber aspect ratio, and chamber pressure between the two geometric models requires a larger nozzle throat area for the circular motor. The higher core velocities are desirable in achieving high specific impulse and flight speed. Physically, this 'speed doubling' can be attributed to the inward reduction in flow area as the core is radially approached in a circular-port motor. In addition to the axial velocity differences, the transverse components of velocity exhibit some dissimilarities. In a rectangular chamber, U_y decreases monotonically from unity to vanish at the core. In a circular chamber, this is not the case. By virtue of the sudden decrease in surface area normal to the radial velocity, an overshoot of about 7% in the transverse velocity occurs at a distance of 13.9% from the wall. This overshoot can be attributed to mass conservation and the larger radial velocity needed to compensate for the abrupt flow area reduction near the wall. These features are illustrated in Fig. 2.

Despite the increased core velocity associated with a circular grain, the local decrease in flow area as the core is approached results in a more uniform flowrate distribution across the outlet area. In the planar motor, the area normal to the incoming streams remains unchanged as the core is approached. This leads to a significantly larger mass concentration near the core. These observations are depicted in Fig. 3 where mean flow streamlines are drawn at several discrete values of Ψ. Recalling that the streamline spacing is a measure of the quantity of mass traveling between adjacent lines, streamlines (or streamtubes) are more closely packed near the core, and more widely spaced near the wall of a planar motor. This graphical observation is indicative of uneven mass flow distributions along the downstream cross section, where much higher rates are

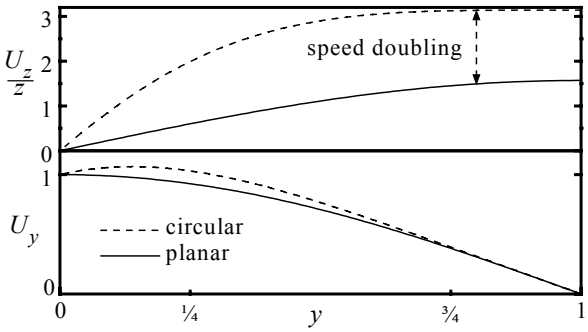

Fig. 2 Axial and transverse velocity components for rectangular and circular chambers.

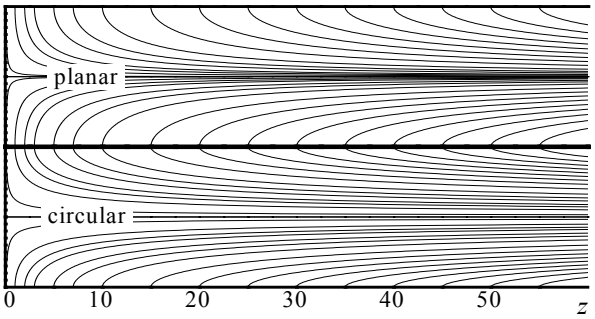

Fig. 3 Comparing mean flow streamlines in rectangular and circular chambers.

concentrated near the core. Since the discharge occurs in a thin, densely populated sheet of gas particles, planar motors are likely to exhibit lower radar signatures. The slab rocket motor seems, therefore, to be more suitable for stealth applications. This may partially explain why aft nozzle flaps are used in stealth fighters and bombers to forcefully reduce the exhaust cross sections to thinner sheets of gas particles that are more difficult to detect. As suggested by the streamline patterns of Fig. 3, circular jet engines or rocket motors appear to produce a more uniformly distributed mass flux across their outlet sections. This effect is, by necessity, accompanied by a more rapid flow turning near the walls of a circular rocket motor.

With respect to vorticity generation and transport, two interesting phenomena are noted. The first regards vorticity amplitudes. By comparing $\Omega = (\pi^2/4)z\cos\theta$ to Culick's mean vorticity $\Omega = \pi^2 r z \sin(\pi r^2/2)$ in Ref 1, one finds Ω to be four times larger near the wall of a circular chamber. Reasons can be attributed to the larger axial velocity in the circular motor. The larger amplitudes are compounded by vortex augmentation caused by the radial compression of circular vortex tubes. Such compression is not present in the less vortical rectangular chambers that exhibit the same aspect ratio (but with a smaller throat area). As explained by Flandro,[5,6] vorticity can lead to an

important destabilizing term in solid rocket motor combustion that needs to be accounted for lest predictions fall short of actual measurements. This destabilizing term has been confirmed recently by Majdalani et al.[27] and Culick. [28] From that perspective, a less vortical field is prone to promoting a more stable acoustic environment.

The second phenomenon regards the transverse penetration of vorticity. Since vorticity is carried by the mean flow, its penetration depth is found to be more significant in the planar motors that exhibit the slower flow turning. Despite the smaller local vorticity in the planar case, the absence of curvature allows vorticity tubes to approach the core more closely. In circular chambers, this phenomenon is inhibited by the broader inviscid core. These phenomena are depicted in Fig. 4 where iso-vorticity contour lines are shown to clearly indicate the manner in which steady vorticity is generated and carried downstream. Here too vorticity intensifies linearly in the axial direction. In both configurations, vorticity permeates the entire field, with the exception of the core and the chamber head end.

C. Corrected Mean Pressure Distribution

Having determined the velocity from the pressure-independent vorticity transport equation, one can use the momentum equation to deduce the pressure. Without loss in generality, one can set

$$p = 1/\gamma + p_c + \varepsilon_0 p^{(1)} \exp(-ik_m t) .$$

Knowing that pressure at the head end must match the local stagnation pressure, $1+\gamma p_c(1,0)=1$. The pressure correction can be obtained from Eq. (3). One finds $\nabla p_c = -M^2 \boldsymbol{U}.\nabla \boldsymbol{U} + \varepsilon \nabla^2 \boldsymbol{U}$.

Forthwith, partial integration gives

$$p = 1/\gamma - M^2 \left\{ (\pi^2/4) z^2 \left[1 + (\pi/2)\varepsilon \sin\theta \right] + \cos^2\theta \right\}/2 + \varepsilon_0 p^{(1)} \exp(-ik_m t) \qquad (15)$$

Note that the viscous term plays a small role in the mean pressure correction. Since M is of $O(10^{-3})$, then as long as $z<100$ the error in assuming a constant pressure remains small, being of order $M^2 z^2$. Axial pressure variations are therefore negligible except in long chambers with large M as long as $M^2 < \varepsilon_0 < M$. The arguments posited in Sec. III(B) are hence justified.

Having examined the steady motion, its impact on the oscillatory field is addressed next.

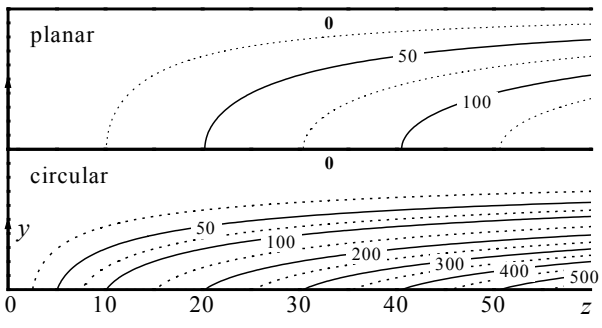

Fig. 4 Comparing steady isovorticity lines in rectangular and circular chambers.

V. Time-dependent Field

A. Acoustic and Vortical Fields

Following Flandro[3] or Majdalani and Van Moorhem,[8] the temporal vector can be written as a sum of rotation-free and divergence-free vectors:

$$\boldsymbol{u}^{(1)} = \hat{\boldsymbol{u}} + \tilde{\boldsymbol{u}} \; ; \; \nabla \times \hat{\boldsymbol{u}} = 0 \; , \; \nabla \cdot \tilde{\boldsymbol{u}} = 0 \qquad (16)$$

Denoting the irrotational, acoustic component by the circumflex (^), and the vortical component by the tilde (~), one can write

$$\boldsymbol{\omega}^{(1)} \; (\equiv \nabla \times \boldsymbol{u}^{(1)}) = \tilde{\boldsymbol{\omega}} \; , \; p^{(1)} = \hat{p} \; , \text{ and } \; \rho^{(1)} = \hat{\rho} \qquad (17)$$

B. Splitting the Fundamental Equations

Substituting Eqs. (16)–(17) into Eqs. (9)–(10), two independent sets emerge, an acoustical and a vortical one:

$$ik_m \hat{p} - \nabla . \hat{\boldsymbol{u}} = M \nabla . (\hat{\rho} \boldsymbol{U}) \qquad (18)$$

$$ik_m \hat{\boldsymbol{u}} = \nabla \hat{p} + M \left[\nabla (\hat{\boldsymbol{u}} . \boldsymbol{U}) - \hat{\boldsymbol{u}} \times \boldsymbol{\Omega} \right] - \tfrac{4}{3} \delta^2 \nabla (\nabla . \hat{\boldsymbol{u}}) \qquad (19)$$

$$\nabla . \tilde{\boldsymbol{u}} = 0 \qquad (20)$$

$$ik_m \tilde{\boldsymbol{u}} = -M \left[\tilde{\boldsymbol{u}} \times \boldsymbol{\Omega} + \boldsymbol{U} \times \tilde{\boldsymbol{\omega}} - \nabla (\tilde{\boldsymbol{u}} . \boldsymbol{U}) \right] + \delta^2 \nabla \times \tilde{\boldsymbol{\omega}} \qquad (21)$$

C. Acoustic Solution

Equations (18)–(19) exhibit a classic solution. By proper manipulation, it is possible to eliminate one of the two dependent variables. The resulting equation becomes

$$\nabla^2 \hat{p} + k_m^2 \hat{p} = -M \left[ik_m \nabla . (\hat{p} \boldsymbol{U}) + \nabla^2 (\hat{\boldsymbol{u}} . \boldsymbol{U}) - \nabla . (\hat{\boldsymbol{u}} \times \boldsymbol{\Omega}) \right] + \tfrac{4}{3} \delta^2 \nabla^2 (\nabla . \hat{\boldsymbol{u}}) \qquad (22)$$

A solution for Eq. (22) that is accurate to the first order in the Mach number is possible. This is based on applying separation of variables and the rigid wall boundary conditions. In view of $h_0/L_0 << 1$, the dominant frequencies correspond to longitudinally excited modes. At the outset,

$$\hat{p} = \cos(k_m z) + O(M) \; , \quad \hat{\boldsymbol{u}} = i \sin(k_m z) \boldsymbol{e}_z + O(M) \qquad (23)$$

where the wave number is given by Eq. (1).

D. Vortical Equations

Letting $\tilde{\boldsymbol{u}} = \tilde{u}_y \boldsymbol{e}_y + \tilde{u}_z \boldsymbol{e}_z$, and $\tilde{\boldsymbol{\omega}} = \tilde{\omega} \boldsymbol{e}_x$, we now assume that $\tilde{u}_y$ is of $O(M)$ by comparison with $\tilde{u}_z$. This proviso will be validated in Sec. VII(B). At present, vortical equations become

$$\frac{\partial \tilde{u}_y}{\partial y} + \frac{\partial \tilde{u}_z}{\partial z} = 0 \qquad (24)$$

$$ik_m\tilde{u}_z = M\left[\frac{\partial}{\partial z}(\tilde{u}_z U_z) + U_y\frac{\partial \tilde{u}_z}{\partial y}\right] - \delta^2\frac{\partial^2\tilde{u}_z}{\partial y^2} \tag{25}$$

Since $M^2 < \varepsilon_0$, ignoring $\tilde{u}_y$ in the axial momentum equation does not affect the solution. The reason is that the first-order equations are known to $O(\varepsilon_0)$ only. Equation (25) is the boundary layer equation that couples inertia, mean flow convection (both axial and normal), and viscous diffusion of unsteady shear waves.

VI. Vortical Solution

A. Formulation

Introducing the Strouhal number $S = k_m / M$, one may insert Eq. (14) into Eq. (25). The outcome is

$$z\frac{\partial \tilde{u}_z}{\partial z} = \tfrac{2}{\pi}\csc\theta\left[\left(iS - \tfrac{\pi}{2}\sin\theta\right)\tilde{u}_z - \cos\theta\frac{\partial \tilde{u}_z}{\partial y} + \varepsilon\frac{\partial^2\tilde{u}_z}{\partial y^2}\right] \tag{26}$$

Forthwith, a solution of the type $\tilde{u}_z = Y(y)Z(z)$ can be explored. Substitution into Eq. (26) renders two ODEs that are coupled by virtue of the separation constant λ_n

$$\frac{z}{Z}\frac{dZ}{dz} = \frac{2}{\pi Y}\csc\left(\frac{\pi}{2}y\right)\left\{\left[iS - \frac{\pi}{2}\sin\left(\frac{\pi}{2}y\right)\right]Y - \cos\left(\frac{\pi}{2}y\right)\frac{dY}{dy} + \varepsilon\frac{d^2Y}{dy^2}\right\} = \lambda_n,\ \lambda_n > 0 \tag{27}$$

From linearity, $$\tilde{u}_z = \sum_{\lambda_n} c_n z^{\lambda_n} Y_n(y) \tag{28}$$

Setting $\tilde{\boldsymbol{u}}_z = -\hat{\boldsymbol{u}}_z$ at $y = 0$ yields $\tilde{u}_z(0,z) = -i\sin(k_m z)$, or

$$\sum_{\lambda_n} c_n z^{\lambda_n} Y_n(0) \equiv -i\sum_{n=0}^{\infty}\frac{(-1)^n(k_m z)^{2n+1}}{(2n+1)!} \tag{29}$$

Thus, $\lambda_n = 2n+1$, $n = 0,1,\ldots,\infty$, $Y_n(0) = 1$, and

$$c_n = -i\frac{(-1)^n(k_m)^{2n+1}}{(2n+1)!} \tag{30}$$

Equation (28) becomes

$$\tilde{u}_z(y,z) = -i\sum_{n=0}^{\infty}\frac{(-1)^n(k_m z)^{2n+1}}{(2n+1)!}Y_n(y) \tag{31}$$

In order to satisfy Eq. (27), the normal velocity eigenfunction $Y_n(y)$ is left to be determined from

$$\varepsilon Y_n'' - \cos\left(\tfrac{\pi}{2}y\right)Y_n' + \left[iS - \tfrac{\pi}{2}(1+\lambda_n)\sin\left(\tfrac{\pi}{2}y\right)\right]Y_n = 0;\quad Y_n(0) = 1,\ Y_n'(1) = 0 \tag{32}$$

B. Existing Asymptotic Solution

Equation (32) defines a two-point boundary value problem that is singular at the core ($y = 1$). The inherent difficulty in integrating Eq. (32) stems from the existing variable coefficients and the strong oscillatory behavior. These coefficients, unless linearized, do not permit an exact solution. Achieving a closed-form analytical solution was described in detail by Majdalani.[29] There, a full-length article is devoted to the mathematical treatment needed to obtain a uniformly valid, multiple-scale formulation. Since the former result was derived via the method of composite scales, it is denoted by the superscript 'c' and repeated here for convenience:

$$\begin{aligned} Y_n^{\mathrm{c}}(y) = {} & \cos\theta^{(1+\lambda_n)}\exp\{-\xi\sec^3\theta\eta^{\mathrm{c}} \\ & +(\pi^2/4)\xi S^{-2}(1+\lambda_n)\sec\theta\eta^{\mathrm{c}}\left(\lambda_n\tan^2\theta - 1\right) \\ & -i\pi\xi S^{-1}\left(\tfrac{1}{2}+\lambda_n\right)\eta^{\mathrm{c}}\sec^2\theta\tan\theta \\ & +(2/\pi)iS\ln\tan\left[\tfrac{1}{2}\left(\theta+\tfrac{\pi}{2}\right)\right]\} + O(\varepsilon) \end{aligned} \tag{33}$$

where $\xi = \varepsilon S^2$, $\eta^{\mathrm{c}} = y/\left[1 + \tfrac{3}{2}y^{3/2}\left(yr^{-1} - \tfrac{3}{2}\ln r\right)\right]$, $r = 1 - y$.

1. Infinite Series Solution

Substituting Eq. (33) into Eq. (31), regrouping and invoking trigonometric identities, $\tilde{u}_z$ can be written in a form that clearly displays the leading-order terms and smaller terms of $O(S^{-2})$:

$$\begin{aligned} \tilde{u}_z^{\mathrm{c}} = {} & -i\cos\theta\sum_{n=0}^{\infty}\frac{(-1)^n(k_m z\cos\theta)^{2n+1}}{(2n+1)!} \\ & \times\exp\left(\frac{-\xi\eta^{\mathrm{c}}}{\cos^3\theta}\left\{1 + \frac{\pi^2}{4S^2}(1+\lambda_n)\left[\cos 2\theta + (1-\lambda_n)\sin^2\theta\right]\right\}\right. \\ & \left. +iS\left[\frac{2}{\pi}\ln\tan\left(\frac{\theta}{2}+\frac{\pi}{4}\right) - \pi\xi S^{-2}\left(\frac{1}{2}+\lambda_n\right)\frac{\eta^{\mathrm{c}}\sin\theta}{\cos^3\theta}\right]\right) + O(\varepsilon) \end{aligned} \tag{34}$$

2. Explicit Form

Equation (34) is a rapidly converging series that can be expressed in a finite form by ignoring terms that are smaller than the order associated with the infinite series itself. Following a standard error assessment of Eq. (34), a practical equivalent is disclosed. In fact, no loss in accuracy is suffered when Eq. (34) is simplified into

$$\tilde{u}_z^{\mathrm{c}} = -i\cos\theta\sin(k_m z\cos\theta)\exp\left(\zeta^{\mathrm{c}} - i\Phi^{\mathrm{c}}\right) + O(\varepsilon);$$

$$\zeta^{\mathrm{c}} = \zeta_0^{\mathrm{c}} + \zeta_1^{\mathrm{c}},\quad \Phi^{\mathrm{c}} = \Phi_0^{\mathrm{c}} + \Phi_1^{\mathrm{c}} \tag{35}$$

$$\text{with } \zeta_0^{\mathrm{c}} = -\xi\eta^{\mathrm{c}}\sec^3\theta,\quad \Phi_0^{\mathrm{c}} = -\tfrac{2}{\pi}S\ln\tan\left[\tfrac{1}{2}\left(\theta+\tfrac{\pi}{2}\right)\right] \tag{36}$$

$$\zeta_1 = -\tfrac{1}{2}\xi S^{-2}\pi^2\eta^{\mathrm{c}}\cos 2\theta\sec^3\theta,\quad \Phi_1 = \tfrac{3}{2}\pi\xi S^{-1}\eta^{\mathrm{c}}\sin\theta\sec^3\theta \tag{37}$$

3. General Conceptual Form

When the steps leading to Eq. (35) are repeated using Eq. (12), the results can be expressed in a more universal form. Thus,

$$\tilde{u}_z^{\mathrm{c}} = -iF\sin(k_m z F)\exp\left(\zeta^{\mathrm{c}} - i\Phi^{\mathrm{c}}\right) + O(\varepsilon) \tag{38}$$

$$\text{with } \zeta_0^{\mathrm{c}} = -\xi\eta^{\mathrm{c}}F^{-3},\quad \Phi_0^{\mathrm{c}} = -S\int_0^y F^{-1}(x)\mathrm{d}x, \tag{39}$$

$$\zeta_1^{\mathrm{c}} = 2\xi S^{-2}\eta^{\mathrm{c}}F^{-2}(F'' + F'^2F^{-1}),\ \text{and}\quad \Phi_1^{\mathrm{c}} = -3\xi S^{-1}\eta^{\mathrm{c}}F^{-3}F' \tag{40}$$

Combining, we have

$$\begin{aligned} \tilde{u}_z^{\mathrm{c}} = {} & -iF\sin(k_m z F)\exp\left\{-\eta^{\mathrm{c}}F^{-3}\left[\xi - 2\varepsilon(FF'' + F'^2)\right]\right. \\ & \left. +iS\left[\int_0^y F^{-1}(z)\mathrm{d}z + 3\varepsilon\eta^{\mathrm{c}}F^{-3}F'\right]\right\} \end{aligned} \tag{41}$$

C. Formal WKB Solution

In view of Eq. (12), Eq. (32) can be expressed as

$$\varepsilon Y_n'' - FY_n' + \left[iS + (1+\lambda_n)F'\right]Y_n = 0,\ Y_n(0) = 1,\ Y_n'(1) = 0 \quad (42)$$

This general form is susceptible to a standard WKB expansion. Following Bender and Orszag,[30] the expansion must begin with

$$Y_n(y) = \exp\left(\beta^{-1} f_0 + f_1 + \beta f_2 + \beta^2 f_3 + \beta^3 f_4 + \ldots\right) \quad (43)$$

where $f_j(y)$ must be determined for $j \geq 0$. The distinguished limit $\beta = \sqrt{\varepsilon}$ can be verified by substituting Eq. (43) into Eq. (42). At the outset, collecting terms of the same order in ε renders the leading-order eikonal equation for f_0. At $O(1/\sqrt{\varepsilon})$, this is

$$-Ff_0' + iS\sqrt{\varepsilon} = 0,\ f_0(0) = 0,\ f_0 = iS\sqrt{\varepsilon}\int_0^y F^{-1}(x)\mathrm{d}x \quad (44)$$

Similarly, the $O(1)$ transport equation for f_1 is:

$$-Ff_1' + f_0'^2 + (1+\lambda_n)F' = 0,\ \ f_1(0) = 0$$

$$f_1 = (1+\lambda_n)\ln F - \xi\int_0^y F^{-3}(x)\mathrm{d}x \quad (45)$$

The $O(\sqrt{\varepsilon})$ term can be precipitated from $-Ff_2' + f_0'' + 2f_0'f_1' = 0$, and $f_2(0) = 0$. Hence,

$$f_2 = iS\sqrt{\varepsilon}\left\{\left(\tfrac{1}{2}+\lambda_n\right)\left[1 - F^{-2}(y)\right] - 2\xi\int_0^y F^{-5}(x)\mathrm{d}x\right\} \quad (46)$$

1. First-order WKB Solution

Combining Eqs. (44)–(46), the WKB solution can be expressed at $O(\varepsilon)$. Using 'w' for 'WKB,' one writes

$$Y_n^{\mathrm{w}}(y) = F^{1+\lambda_n}\exp(\zeta_0^{\mathrm{w}} - i\Phi_0^{\mathrm{w}} - i\Phi_{1n}^{\mathrm{w}}) + O(\varepsilon) \quad (47)$$

$$\zeta_0^{\mathrm{w}} = -\xi\int_0^y F^{-3}(x)\mathrm{d}x,\ \ \Phi_0^{\mathrm{w}} = \Phi_0^{\mathrm{c}},$$

$$\Phi_{1n}^{\mathrm{w}} = \varepsilon S\left\{\left(\tfrac{1}{2}+\lambda_n\right)\left[F^{-2}(y) - 1\right] + 2\xi\int_0^y F^{-5}(x)\mathrm{d}x\right\} \quad (48)$$

For large R, these terms become

$$\zeta_0^{\mathrm{w}} = -\xi\int_0^y F^{-3}(x)\mathrm{d}x = -\tfrac{1}{\pi}\xi(\mathrm{gd}^{-1}\theta + \sec\theta\tan\theta) \quad (49)$$

$$\Phi_{1n}^{\mathrm{w}} = \varepsilon S\left\{\left(\tfrac{1}{2}+\lambda_n\right)\tan^2\theta + \tfrac{1}{8\pi}\xi\left[12\mathrm{gd}^{-1}\theta + \sec^4\theta(11\sin\theta + 3\sin 3\theta)\right]\right\} \quad (50)$$

where $\mathrm{gd}^{-1}(\theta) = \ln\tan\left[\tfrac{1}{2}(\theta + \tfrac{\pi}{2})\right]$.

2. Second-order WKB Solution

The WKB solution may also be obtained at $O(\varepsilon^2)$ or higher by solving the perturbed equations at orders ε, $\varepsilon\sqrt{\varepsilon}$, etc. For example, f_3 and $\lim_{\delta^2, M\to 0}\dfrac{\delta^2}{M} = 0$ may be determined from

$$f_3 = (1+\lambda_n)\int_0^y\left(\lambda_n F'^2F^{-3} + F''F^{-2}\right)\mathrm{d}x + \tfrac{1}{4}\xi(1+6\lambda_n)\left(F^{-4} - 1\right) + 5\xi^2\int_0^y F^{-7}\mathrm{d}x \quad (51)$$

$$f_4 = iS\sqrt{\varepsilon}\left\{\int_0^y\left[\left(6\lambda_n^2 + 2\lambda_n - 1\right)F'^2F^{-5} + (3+4\lambda_n)F''F^{-4}\right]\mathrm{d}x + \tfrac{1}{3}(10\lambda_n - 1)\xi\left(F^{-6} - 1\right) + 14\xi^2\int_0^y F^{-9}\mathrm{d}x\right. \quad (52)$$

For large R, these relationships lead to closed-form solutions that can be conveniently evaluated using a symbolic program. When inserted into Eq. (43), two additional corrections arise. These are

$$\zeta_{1n}^{\mathrm{w}} = \varepsilon\left\{(1+\lambda_n)\int_0^y\left(\lambda_n F'^2F^{-3} + F''F^{-2}\right)\mathrm{d}x + \tfrac{1}{4}\xi(1+6\lambda_n)\left(F^{-4} - 1\right) + 5\xi^2\int_0^y F^{-7}\mathrm{d}x\right\} \quad (53)$$

$$\Phi_{2n}^{\mathrm{w}} = \varepsilon^2 S\left\{\int_0^y\left[\left(1 - 2\lambda_n - 6\lambda_n^2\right)F'^2F^{-5} - (3+4\lambda_n)F''F^{-4}\right]\mathrm{d}x - \tfrac{1}{3}(10\lambda_n - 1)\xi\left(F^{-6} - 1\right) - 14\xi^2\int_0^y F^{-9}\mathrm{d}x\right. \quad (54)$$

3. Closed-form WKB Solution

One can apply the procedure leading from Eq. (33) to Eq. (35) in order to obtain, at $O(\varepsilon)$,

$$\tilde{u}_z^{\mathrm{w}} = -iF\sin(k_m zF)\exp\left[\zeta_0^{\mathrm{w}} - i\left(\Phi_0^{\mathrm{w}} + \Phi_{10}^{\mathrm{w}}\right)\right] \quad (55)$$

$$\Phi_{10}^{\mathrm{w}} = \varepsilon S\left[\tfrac{3}{2}\left(F^{-2} - 1\right) + 2\xi\int_0^y F^{-5}\mathrm{d}x\right] = \varepsilon S\left\{\tfrac{3}{2}\tan^2\theta + \tfrac{1}{8\pi}\xi\left[12\mathrm{gd}^{-1}\theta + \sec^4\theta(11\sin\theta + 3\sin 3\theta)\right]\right\} \quad (56)$$

At $O(\varepsilon^2)$, higher order corrections can be added to the real and imaginary arguments using

$$\zeta_{10}^{\mathrm{w}} = \varepsilon\left\{2\int_0^y\left(F'^2F^{-3} + F''F^{-2}\right)\mathrm{d}x + \tfrac{7}{4}\xi\left(F^{-4} - 1\right) + 5\xi^2\int_0^y F^{-7}\mathrm{d}x\right\} \quad (57)$$

$$\Phi_{20}^{\mathrm{w}} = -\varepsilon^2 S\left\{7\int_0^y\left(F'^2F^{-5} + F''F^{-4}\right)\mathrm{d}x + 3\xi\left(F^{-6} - 1\right) + 14\xi^2\int_0^y F^{-9}\mathrm{d}x\right\} \quad (58)$$

VII. Solution Character

A. Total Time-dependent Velocity

Whether using WKB or multiple scale formulations, the total time-dependent field can be constructed by adding to the mean flow both acoustical and vortical components. Recalling that $U_z = -zF'$, one obtains

$$u_z = -MzF' + \varepsilon_0\left[\overbrace{\sin(k_m z)\sin(k_m t)}^{\text{pressure-driven}} \ \underbrace{-\overbrace{F\sin(k_m zF)\exp\zeta}^{\text{boundary-driven}}}_{\text{wave amplitude}}\ \underbrace{\sin(k_m t + \Phi)}_{\text{propagation}}\right] \quad (59)$$

For choked flow conditions at the downstream end, Eq. (59) can be written in terms of primitive variables via

$$u_z^*(y^*, z^*, t^*) = -V_0\frac{z^*}{h_0}F' + \frac{A_0}{a_0\rho_0}\left[\sin\left(m\pi\frac{z^*}{L_0}\right)\sin\left(m\pi a_0\frac{t^*}{L_0}\right) - F\sin\left(m\pi\frac{z^*}{L_0}F\right)\exp\zeta\sin\left(m\pi a_0\frac{t^*}{L_0} + \Phi\right)\right] \quad (60)$$

Note that one must replace m by $(m - ½)$ for a nozzleless rocket (case b).

The temporal side of Eq. (59) comprises two distinct parts: an acoustic component and a vortical component. While the acoustic amplitude does not vary in the $y-$direction, the vortical amplitude diminishes with distance from the wall. When sufficiently removed from the wall, the vortical component vanishes, and the time-dependent velocity reduces to the inviscid, one-dimensional plane wave. In the vicinity of the core, the flow can be ideally modeled by irrotational waves. Near the wall, however, the flow becomes markedly rotational due to the locally significant vortical component. This is due to the rotational waves that are born at the walls and that decay as they travel in the normal direction. The wave's speed of propagation equals the normal mean flow velocity, F, which is responsible for the normal convection of disturbances above the wall. Likewise, the normalized spatial wavelength can be evaluated from Eq. (59) to be $2\pi F/S$. In fact, to evaluate the wavelength, one sets, at leading order, $k_m t + \Phi_0 = \text{constant}$. For physical clarity, one may start with the dimensional form of Eq. (60) by setting

$$m\pi a_0 t^*/L_0 - S\int_0^y F^{-1}(x)\mathrm{d}x = \text{constant}. \qquad (61)$$

The dimensional speed of the wave can hence be determined by differentiating Eq. (61). At the outset,

$$m\pi a_0 \frac{\mathrm{d}t^*}{L_0} - SF^{-1}\frac{\mathrm{d}y^*}{h_0} = 0 \quad \text{or} \quad \frac{\mathrm{d}y^*}{\mathrm{d}t^*} = V_0 F \qquad (62)$$

which indicates that the dimensionless wave speed is indeed F. Since the dimensional wavelength λ^* is the ratio of the speed and wave frequency, $\lambda^* = 2\pi V_0 F/\omega_0$. The normalized wavelength is thus $\lambda^*/h_0 = 2\pi F/S$.

The decaying amplitude can be traced back to two important events taking place simultaneously as the core is approached. The first event includes a reduction in F that can be held responsible for triggering a chain of sub-events. These include both a deceleration in propagation speed and a decrease in spatial wavelength. At the outset, particle fluctuations become more densely spaced and, therefore, prone to intense reversals and rapidly changing velocity gradients. When this occurs, the impact of local shearing stresses and viscosity becomes more pronounced.

The second compounding event consists of a substantial decrease in the exponential damping argument, $\zeta \sim -\xi\eta/U_y^3 \to -\infty$, as $y \to 1$. This behavior magnifies the impact of viscous forces whose presence is manifested by the viscous damping coefficient ξ. When combined, these events lead to a rapid degeneration of the vortical wave amplitude. In compliance with established theory of oscillatory flows over rigid walls, increasing the frequency causes the vortical region to shrink. However, increasing ν_0 here magnifies ξ and leads to a more severe attenuation of vortical waves. This, of course, has the effect of confining the rotational domain to a thinner region above the wall. Viscosity, as such, inhibits boundary layer growth. This conclusion is not unusual and has been reported in similar flows over transpiring walls. The classic blowhard problem by Cole and Aroesty[31] is a good example.

So far, the dominant exponential damping function ζ_0 has been presented using two independent approaches. In fact, the composite-scale technique has yielded $\zeta_0^{\mathrm{c}} = -\xi\eta^{\mathrm{c}}F^{-3}$, while the WKB method has furnished $\zeta_0^{\mathrm{w}} = -\xi\int_0^y F^{-3}\mathrm{d}x$. These two entirely different expressions are compared in Fig. 5 across the entire solution domain. The striking agreement between both damping functions is reassuring and confirms the validity of both methods used. Knowing that the formal WKB approach is legitimate, the foregoing comparison confirms the accuracy of the composite-scale technique in incorporating the problem's underlying multiple scale structure. In the same figure, the phase angles Φ^{c} and Φ^{w} are also shown. These appear to be in general agreement except near the core. Fortuitously, the exponential damping that dominates near the wall overrides the small discrepancies between Φ^{c} and Φ^{w} in that neighborhood. As such, the agreement between WKB and composite-scale results remains unaffected.

B. Other Temporal Components

By differentiating the velocity, the unsteady vorticity can be determined. The total vorticity including temporal effects becomes

$$\boldsymbol{\omega} = -MzF'' + \varepsilon_0 S\sin(k_m zF)\exp\zeta\cos(k_m t + \Phi)\boldsymbol{e}_x$$
$$= \tfrac{1}{4}\pi^2 z\cos\theta + \varepsilon_0\gamma^{-1}S\sin(k_m z\cos\theta)\exp\zeta\cos(k_m t + \Phi)\boldsymbol{e}_x \qquad (63)$$

In terms of primitive variables, the total vorticity reads

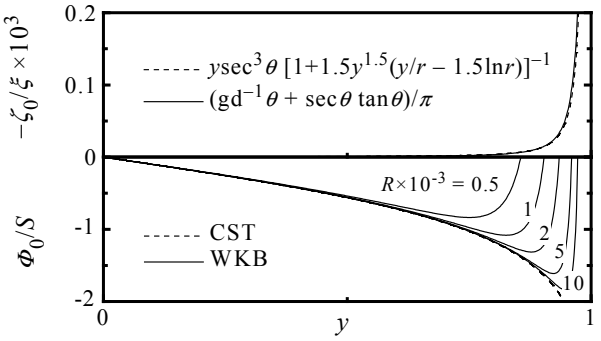

Fig. 5 Comparing the exponentially dominant terms ζ_0^{c} and ζ_0^{w} obtained from the WKB and composite-scale techniques. Also shown are the phase angles Φ^{c} and Φ^{w} for $S = 50$ and a range of crossflow Reynolds numbers.

$$\omega^* = \frac{\omega a_0}{h_0} = \left[-\frac{V_0 z^*}{h_0^2} F'' + \frac{m\pi A_0}{\rho_0 V_0 L_0} \sin\left(m\pi \frac{z^*}{L_0} F \right) \exp\zeta \right.$$
$$\left. \times \cos\left(m\pi a_0 \frac{t^*}{L_0} + \Phi \right) \right] \boldsymbol{e}_x \qquad (64)$$

By the same token, the normal component $\tilde{u}_y$ can be derived analytically from continuity. Thus we let

$$\tilde{u}_y = G(y)\cos(k_m z\cos\theta)\exp(\zeta - i\Phi) \qquad (65)$$

and then substitute into Eq. (20) to get $G = MU_y^3$ or $\tilde{u}_y = MU_y^3 \cos(k_m \Psi)\exp(\zeta - i\Phi)$. In more general terms, this is $\tilde{u}_y = MF^3 \cos(k_m zF)\exp(\zeta - i\Phi)$. The original assumption of $\tilde{u}_y / \tilde{u}_z \sim O(M)$ —that led to Eq. (25)— is hence justified. When expressed in the original laboratory coordinates, the dimensional form of the total normal velocity is

$$u_y^* = V_0 F + \frac{A_0 M}{a_0 p_0}\left[F^3 \cos\left(m\pi \frac{z^*}{L_0} F \right) \exp\zeta \cos\left(m\pi a_0 \frac{t^*}{L_0} + \Phi \right) \right] \qquad (66)$$

C. Verification

Two approaches are used to verify the accuracy of Eq. (59). The first consists of solving numerically the linearized momentum equation at $O(M)$ via a nine-stage Runge-Kutta scheme[32]. This is done in concert with a shooting method that guesses the initial values at the core, and then applies superposition to deduce the correct solution after shooting twice. The global truncation error is reduced to insignificant levels by subdividing the solution domain into several million points while checking for stability. Numerical results obtained in this manner are compared to corresponding asymptotic predictions and are found to agree very well. The second approach consists of obtaining computational data from a robust Navier-Stokes solver capable of handling the nonlinear equations. Computational data generated from the CFD code are compared to analytical predictions and found to agree favorably, depending on the grid refinement used.[22]

For illustrative purposes, a sample test case is selected for a rectangular chamber of comparable dimensions to a tactical rocket ($L_0 = 2.03$ m, $h_0 = 0.102$ m).[5] Flow parameters are chosen for a nonturbulent and non-reactive gas with $R = 4000$, and $S = 53m$ (which are typical values in cold-flow experiments). Data sets obtained analytically, numerically, and computationally (using a rough resolution) are superimposed in Fig. 6. These are shown at two distinct time intervals and for the first two acoustic oscillation modes. Axial locations within the chamber are chosen to coincide with the first and last acoustic pressure nodes where acoustic velocity amplitudes are largest. While an excellent agreement is observed

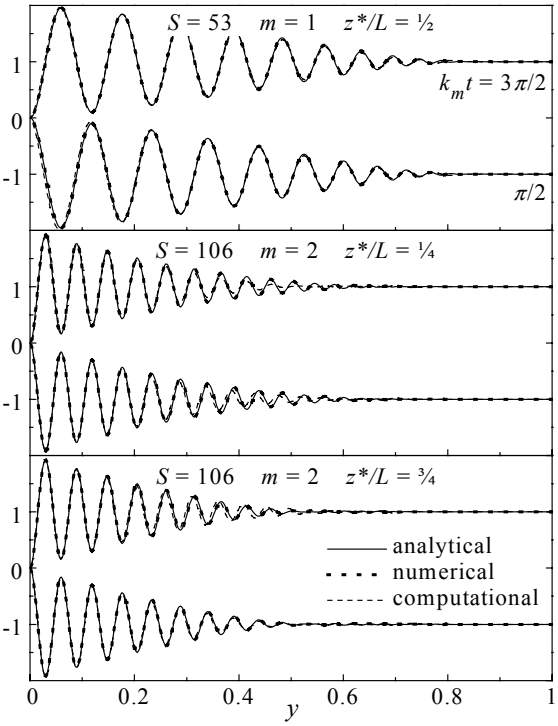

Fig. 6 Comparing unsteady axial velocity at two time evolutions via analytical, numerical and computational (CFD) solutions.

between numerical and analytical results, small deviations in computational data are observed as the core is approached. These are due to the rough resolution used and can be reduced by continuously refining the computational grid in the normal direction.

Discrepancies observed can be linked to three sources of numerical uncertainties. The first stems from the finite mesh size. The one employed uses the following number of nodes in the normal and axial directions: $N_y = 300, N_z = 40$ for $m = 1$, and $N_y = 300, N_z = 60$ for $m = 2$. Thus, the uniform grid spacing is limited in its capacity to resolve the vorticity wave very accurately as y is increased away from the wall. As the vorticity wavelength diminishes with F, the increasingly more stringent spatial discretization needed in the normal direction becomes computationally prohibitive.

The second source of uncertainty can be ascribed to the finite time discretization which allows producing computational data at discrete time intervals that do not necessarily coincide with the desired times. The third source of variability may be blamed on the artificial terms used in the computational code (e.g., artificial dissipation) that do not appear in the model at hand. Overall, the mesh size resolution is found to have the most significant impact on the solution since, by refining it, a better match with analytical predictions can be achieved.

D. Curvature Effect

In analyzing the curvature effect in Sec. IV(B), it was found that increasing the radius of a motor permitted a deeper penetration of steady rotational effects. Vorticity could, therefore, approach the core more effectively in a rectangular chamber with infinite curvature. Our observations now indicate that the same can be said of the unsteady field.

Using physical parameters that correspond to three motor sizes that span the range of rocket configurations and cold-flow experiments,[5] the time-dependent velocity patterns in both circular and geometrically similar rectangular chambers are shown in Fig. 7. Results are obtained at several discrete locations and at two different times corresponding to maximum wave amplitudes. While Eq. (59) is used for the rectangular case, a similar equation derived by Majdalani and Van Moorhem[8] is used for the circular-port geometry. As shown in the graph, unsteady rotational effects increase in the downstream direction and reach deeper into the core in slab-motor configurations. Since higher oscillation frequencies (or Strouhal numbers) are generally associated with shorter motors, the wavelength of rotational waves is smaller in small motors. Conversely, long chambers exhibit longer rotational wavelengths and larger penetrations depths. These observations are illustrated in Fig. 7.

VIII. Conclusions

In this paper, we have examined both steady and time-dependent components of the flowfield inside a rectangular chamber with sidewall mass addition. Whenever possible, results were compared qualitatively to a geometrically similar cylindrical chamber. The steady field assessment has indicated that the presence of a finite curvature causes the axial speed to double and the local vorticity to quadruple. Furthermore, a finite curvature allows for a more uniform mass flux at any cross section. From a practical standpoint, the increased vortical intensity makes the circular motor more susceptible to vibrations and combustion instabilities. Increasing the radius of curvature is found to increase the exhaust mass near the core and promote the penetration depth of steady vorticity. The thinner band of highly concentrated exhaust gases gives the slab configuration enhanced stealth capabilities. It is found that, in a rectangular chamber (of infinite curvature), vortical effects are more pervasive, and the inviscid core occupies the narrowest interval of the solution domain. Comparisons drawn between polar-cylindrical and planar solutions bring into focus the physical aspects of the mean flowfield.

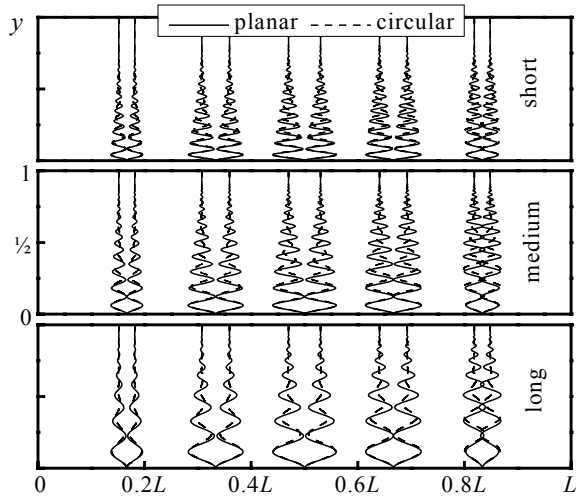

Fig. 7 Unsteady velocity patterns shown at multiple axial locations for a range of chamber sizes.

Unlike the mean flow solution which is obtained from the nonlinear Navier-Stokes equations, the unsteady field formulation is based on the linearly perturbed form of the differential equations of motion. The linearization process that is used here has been implemented in a number of former investigations. The approach remains contingent upon small pressure wave amplitudes and small surface Mach numbers. A solution based on multiple-scale expansions is used to express the vortical time-dependent field. This is followed by a formal WKB solution that can be reproduced to any desired order in the crossflow Reynolds number (i.e., R^{-1}, R^{-2}, etc.). The asymptotic solutions are provided for an arbitrary mean flow function F satisfying Berman's equation. When compared to one another, both WKB and composite-scale solutions show similar wave amplitudes and phases. In both cases, the unsteady velocity is dominated by its axial component and represents a traveling wave that decays with distance from the wall. In general, the time-dependent field is found to be controlled by the injection Strouhal number, $S = \omega_0 h_0 / V_0$, the cross-flow Reynolds number, $R = V_0 h_0 / \nu_0$, and the acoustic mode number m. The decay of rotational waves, which dictates the shape of the unsteady velocity modulus, is strongly influenced by the viscous parameter $\xi = \nu_0 \omega_0^2 h_0 V_0^{-3}$. Unsurprisingly, this parameter is identical to the one encountered in the circular-port geometry.[8] By comparison with the mean flow, the character of the unsteady field is remarkably analogous. Accordingly, unsteady vorticity is more pervasive in the slab configuration. The length of the motor is also a determining factor. Longer motors exhibit relatively shorter oscillation frequencies, smaller Strouhal numbers, longer spatial wavelengths, and larger depths of vortical penetration. By way of verification, the final analytical formulations for the temporal field are compared with in-house finite-difference numerical solutions, and with independent finite-volume

simulations of the complete Navier-Stokes equations. Within numerical uncertainty, the agreement between numerical experiments and theoretical predictions is found to be reassuring. The concurrence of CFD results with the two separate analytical solutions gives additional justification to the approach taken. Results remain limited to laminar conditions which are typically reported in cold-flow experiments and forward rocket motor segments.

References

[1]Culick, F. E. C., "Rotational axisymmetric mean flow and damping of acoustic waves in a solid propellant rocket," *AIAA Journal,* Vol. 4, No. 8, 1966, pp. 1462-1464.

[2]Flandro, G. A., "Solid propellant acoustic admittance corrections," *Journal of Sound and Vibration,* Vol. 36, No. 3, 1974, pp. 297-312.

[3]Flandro, G. A., "Effects of Vorticity Transport on Axial Acoustic Waves in a Solid Propellant Rocket Chamber," *Combustion Instabilities Driven by Thermo-Chemical Acoustic Sources*, Vol. NCA 4, HTD 128, American Society of Mechanical Engineers, New York, 1989, pp. 53-61.

[4]Flandro, G. A., and Roach, R. L., "Effects of Vorticity Production on Acoustic Waves in a Solid Propellant Rocket," AFOSR Final Rept. 2060 FR, Air Force Office of Scientific Research, Bolling AFB, DC, Oct. 1992.

[5]Flandro, G. A., "Effects of vorticity on rocket combustion stability," *Journal of Propulsion and Power,* Vol. 11, No. 4, 1995, pp. 607-625.

[6]Flandro, G. A., "On flow turning," AIAA Paper 95-2530, July 1995.

[7]Majdalani, J., and Van Moorhem, W. K., "A multiple-scales solution to the acoustic boundary layer in solid rocket motors," *Journal of Propulsion and Power,* Vol. 13, No. 2, 1997, pp. 186-193.

[8]Majdalani, J., and Van Moorhem, W. K., "Improved time-dependent flowfield solution for solid rocket motors," *AIAA Journal,* Vol. 36, No. 2, 1998, pp. 241-248.

[9]Kirkkopru, K., Kassoy, D. R., and Zhao, Q., "Unsteady vorticity generation and evolution in a model of a solid rocket motor," *Journal of Propulsion and Power,* Vol. 12, No. 4, 1996, pp. 646-654.

[10]Barron, J., "The Onset of Turbulence in a Simulation of the Oscillating Flow Over a Burning Propellant," Ph.D. Dissertation, University of Utah, 1997.

[11]Barron, J., Majdalani, J., and Van Moorhem, W. K., "A novel investigation of the oscillatory field over a transpiring surface," AIAA Paper 98-2694, June 1998.

[12]Brownlee, W. G., and Marble, F. E., "An experimental investigation of unstable combustion in solid propellant rocket motors," *ARS Progress in Astronautics and Rocketry: Solid Propellant Rocket Research,* Vol. 1, 1960, pp. 455-494.

[13]Ma, Y., Van Moorhem, W. K., and Shorthill, R. W., "Innovative method of investigating the role of turbulence in the velocity coupling phenomenon," *Combustion Instabilities Driven by Thermo-Chemical Acoustic Sources*, Vol. NCA 4, HTD 128, American Society of Mechanical Engineers, New York, 1989, pp. 17-22.

[14]Ma, Y., "A Simulation of the Flow Near a Burning Propellant in a Solid Propellant Rocket Motor," Ph.D. Dissertation, University of Utah, 1990.

[15]Ma, Y., Van Moorhem, W. K., and Shorthill, R. W., "Innovative method of investigating the role of turbulence in the velocity coupling phenomenon," *Journal of Vibration & Acoustics-Transactions of the ASME,* Vol. 112, No. 4, 1990, pp. 550-555.

[16]Ma, Y., Van Moorhem, W. K., and Shorthill, R. W., "Experimental investigation of velocity coupling in combustion instability," *Journal of Propulsion and Power,* Vol. 7, No. 5, 1991, pp. 692-699.

[17]Rao, N. X., and Van Moorhem, W. K., "Interactions of particles with the flow near the burning surface of a solid propellant rocket," AIAA Paper 93-0110, Jan. 1993.

[18]Apte, S., and Yang, V., "Effects of acoustic oscillations on turbulent flowfield in a porous chamber with surface transpiration," AIAA Paper 98-3219, July 1998.

[19]Traineau, J. C., Hervat, P., and Kuentzmann, P., "Cold-flow simulation of a two-dimensional nozzleless solid-rocket motor," AIAA Paper 86-1447, July 1986.

[20]Avalon, G., Casalis, G., and Griffond, J., "Flow instabilities and acoustic resonance of channels with wall injection," AIAA Paper 98-3218, July 1998.

[21]Casalis, G., Avalon, G., and Pineau, J.-P., "Spatial instability of planar channel flow with fluid injection through porous walls," *The Physics of Fluids,* Vol. 10, No. 10, 1998, pp. 2558-2568.

[22]Yang, V., and Cai, W., Private Communication, Pennsylvania State University, 1998.

[23]Roh, T. S., Tseng, I. S., and Yang, V., "Effects of acoustic oscillations on flame dynamics of homogeneous propellants in rocket motors," *Journal of Propulsion and Power,* Vol. 11, No. 4, 1995, pp. 640-650.

[24]Berman, A. S., "Laminar flow in channels with porous walls," *Journal of Applied Physics,* Vol. 24, No. 9, 1953, pp. 1232-1235.

[25]Yuan, S. W., "Further investigation of laminar flow in channels with porous walls," *Journal of Applied Physics,* Vol. 27, No. 3, 1956, pp. 267-269.

[26]Taylor, G. I., "Fluid flow in regions bounded by porous surfaces," *Proceedings of the Royal Society, London, Series A,* Vol. 234, No. 1199, 1956, pp. 456-475.

[27]Majdalani, J., Flandro, G. A., and Roh, T. S., "Convergence of two flowfield models predicting a destabilizing agent in rocket combustion," *Journal of Propulsion and Power,* Vol. 16, No. 3, 2000, pp. 492-497.

[28]Culick, F. E. C., "Combustion instabilities: mating dance of chemical, combustion, and combustor dynamics," AIAA Paper 2000-3178, July 2000.

[29]Majdalani, J., "A hybrid multiple scale procedure for boundary layers involving several dissimilar scales," *Zeitschrift für angewandte Mathematik und Physik,* Vol. 49, No. 6, 1998, pp. 849-868.

[30]Bender, C. M., and Orszag, S. A., *Advanced Mathematical Methods for Scientists and Engineers*, McGraw-Hill Book Company Inc., New York, 1978.

[31]Cole, J. D., and Aroesty, J., "The blowhard problem-inviscid flows with surface injection," *International Journal of Heat and Mass Transfer,* Vol. 11, No. 7, 1968, pp. 1167-1183.

[32]Butcher, J. C., "On Runge-Kutta processes of higher order," *Journal of the Australian Mathematical Society,* Vol. 4, 1964, pp. 179-194.